

Research Paper

Cite this article: Dietz M, Bauch A, Aufinger K, Weigel R, Hagelauer A (2018). A 1 to 32 GHz broadband multi-octave receiver for monolithic integrated vector network analyzers in SiGe technology. *International Journal of Microwave and Wireless Technologies* **10**, 717–728. <https://doi.org/10.1017/S175907871800079X>

Received: 17 September 2017

Revised: 25 April 2018

Accepted: 30 April 2018

First published online: 28 June 2018

Key words:

active circuits; RF front-ends; ultra broadband receiver

Author for correspondence:

Marco Dietz, E-mail: marco.dietz@fau.de

A 1 to 32 GHz broadband multi-octave receiver for monolithic integrated vector network analyzers in SiGe technology

Marco Dietz¹, Andreas Bauch¹, Klaus Aufinger², Robert Weigel¹
and Amelie Hagelauer¹

¹Institute for Electronics Engineering, Friedrich-Alexander-University Erlangen-Nuremberg, Cauerstr. 9, 91058 Erlangen, Germany and ²Infineon Technologies AG, Am Campeon 1-12, 85579 Neubiberg, Germany

Abstract

A multi-octave receiver chain is presented for the use in a monolithic integrated vector network analyzer. The receiver exhibits a very wide frequency range of 1–32 GHz, where the gain meets the 3 dB-criterion. The differential receiver consists of an ultra-wideband low noise amplifier, an active mixer and an output buffer and exhibits a maximum conversion gain (CG) of 16.6 dB. The main design goal is a very flat CG over five octaves, which eases calibration of the monolithic integrated vector network analyzer. To realize variable gain functionality, without losing much input matching, an extended gain control circuit with additional feedback branch is shown. For the maximum gain level, a matching better than –10 dB is achieved between 1–28 GHz, and up to 30.5 GHz the matching is better than –8.4 dB. For both, the input matching and the gain of the LNA, the influence of the fabrication tolerances are investigated. A second gain control is implemented to improve isolation. The measured isolations between RF-to-LO and LO-to-RF are better than 30 dB and 60 dB, respectively. The LO-to-IF isolation is better than 35 dB. The noise figure of the broadband receiver is between 4.6 and 5.8 dB for 4–32 GHz and the output referred 1-dB-compression-point varies from 0.1 to 4.3 dBm from 2–32 GHz. The receiver draws a current of max. 66 mA at 3.3 V.

Introduction

In recent years, the need for integrated sensors has increased. A reason is the novel trend of Internet of Things (IoT), which allows completely new applications and opportunities in the industrial and in the upcoming biomedical area [1]. In connection with IoT, wearables with biomedical focus are a new application, which needs integrated sensors. Wearables can be used to detect many different vital parameters. This allows a very precise image of the current state of health of the user. With the identification of the composition of biological tissues inside the human body, a more accurate analysis of the user's condition is possible [1]. For the future, a promising approach are non-invasive microwave biosensors, which use electromagnetic waves for detection of the vital parameters. This approach is preferable for wearables, because of its non-invasive measurement principle and the compact size. Microwave sensors are well suited not only for biological application but also for the characterization in industrial surroundings, where they open completely new opportunities. For example, microwave sensors enable robots to perceive their near surrounding in this way that they can distinguish biological materials from other materials. This is important e.g. for the interaction with humans. One often used class of microwave sensors are broadband sensors, like open waveguide sensors or the coaxial probe [1]. They exhibit a bandwidth over a frequency range of several GHz. A possible readout device for this kind of sensors are monolithically integrated vector network analyzers (VNA) [2]. For the translation of such broadband signals to a much lower fixed intermediate frequency, a multi-octave receiver front-end is necessary. This paper presents a receiver with a frequency range of 1–32 GHz. Such a high input bandwidth demands several bandwidth-extensions for reaching both, a well-matched input of the receiver over the whole bandwidth, as well as a high and flat gain-function. Both are necessary for the quality of the measurement performance of the integrated VNA, as well as for an accurate calibration. Furthermore, an enhanced gain control functionality is essential to handle the very different power levels of the measured input signal, but without the loss of input matching for decreased gain levels, as it is the case of standard gain control circuits.

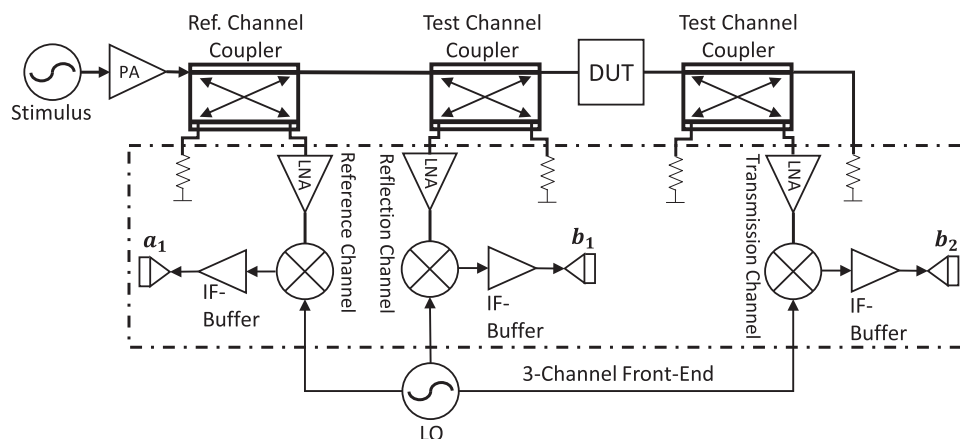


Fig. 1. Simplified representation of a 2-port VNA with 3 receiver channels based on [2, 5].

SiGe technology

The shown receiver components are realized in the B7HF200 SiGe technology, a 0.35 μm bipolar technology from Infineon Technologies AG [3]. For active circuits, three different types of NPN transistor are available: the ultra high speed (UHS), the high speed (HS), and the high voltage (HV). In addition, high-performance varactors are available for active circuits [4]. Furthermore, three types of resistors can be used. Besides two poly resistors with sheet resistances of 1000 Ω/sq and 150 Ω/sq , a TaN thin film resistor can be used, which has a sheet resistance of 20 Ω/sq . The B7HF200 technology offers four copper metalization layers with thicknesses of 600, 600, 1200, and 2500 nm, respectively [3]. The upper layer with 2500 nm is predestined for passive structures, like spiral inductors, which benefit from the low resistivity due to the high cross-section of the upper metal layer. This allows inductances with a high-quality factor. Also, a metal-insulator-metal (MIM)-capacitor is included in the four-layer metal stack.

System overview

3-Channel front-end

For the use in a monolithic integrated VNA, which can determine the reflection- and the transmission-coefficients of a DUT, a front-end with minimum three or more receiver chains is necessary. A simplified representation of a 2-Port VNA is shown in Fig. 1, which is based on [2, 5]. For the measuring of complex S-Parameters, besides the determination of the amplitude, the phase has to be detected. Therefore, a comparison between the phase of the stimulus and the phase of the reflected or transmitted signal, respectively, has to be done, in addition to the comparison of the magnitudes. This requires an additional receiver, which measures the stimulus signal. This additional receiver chain is typically named as reference channel (see Fig. 1) and allows a vectorial measurement of the S-Parameters. It is important to use a coherent receiver architecture, to get both, the magnitude and the phase of the received signal portion [2]. Since the quality of the S-Parameter measurements depends directly on the quantity of the signal portion of the respective test channel and of the reference signal, it is obvious that any superposition through crosstalk or feedthrough has to be avoided. Therefore, the isolation between the receiver chains has to be as high as possible, as well as the isolation inside a receiver chain [5].

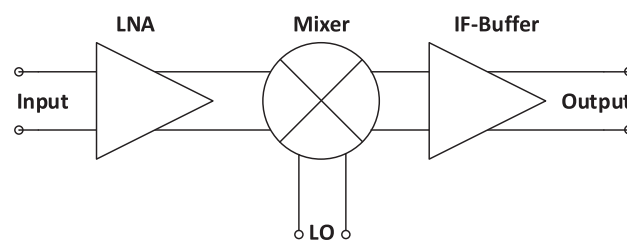


Fig. 2. System overview of the presented broadband receiver. It consists of a LNA and an active mixer with an integrated IF output buffer.

Multi-octave receiver chain

The realized receiver chain consists of an ultra-broadband low noise amplifier (LNA), followed by a broadband active mixer with an integrated IF buffer, which is shown in Fig. 2. The proposed receiver is based on a heterodyne architecture with an IF frequency of 1 GHz. In the context of biological test material, the variable gain control circuit (VGC) of the LNA is realized with an additional shunt feedback in the VGC circuit, to achieve an adequate input matching for all adjusted gain levels. This is a special added extension for the use case of the receiver in a VNA. The advantage of this topology is that low gain levels do not result in input mismatch of the receiver. This prevents multiple reflections between the test port of the VNA and a bad matched DUT, like it is often the case for biological materials. The LNA exhibits a second variable-gain functionality on its output, to improve the tuning precision and the isolation of the receiver chain if it is turned off. Furthermore, the second gain control function is necessary, to enable a precise handling of very different input power levels, which are typical for biomedical applications. This allows a very accurate regulation of output power level for the next receiver stages.

Circuit design

LNA

For achieving the enormous bandwidth from 1 to 32 GHz, several techniques must be used to get a high and flat gain over this frequency range, as well as a good input matching and a low noise figure at the same time. If only one bandwidth extension method is used, especially the 3 dB-criterion of the gain would be exceeded.

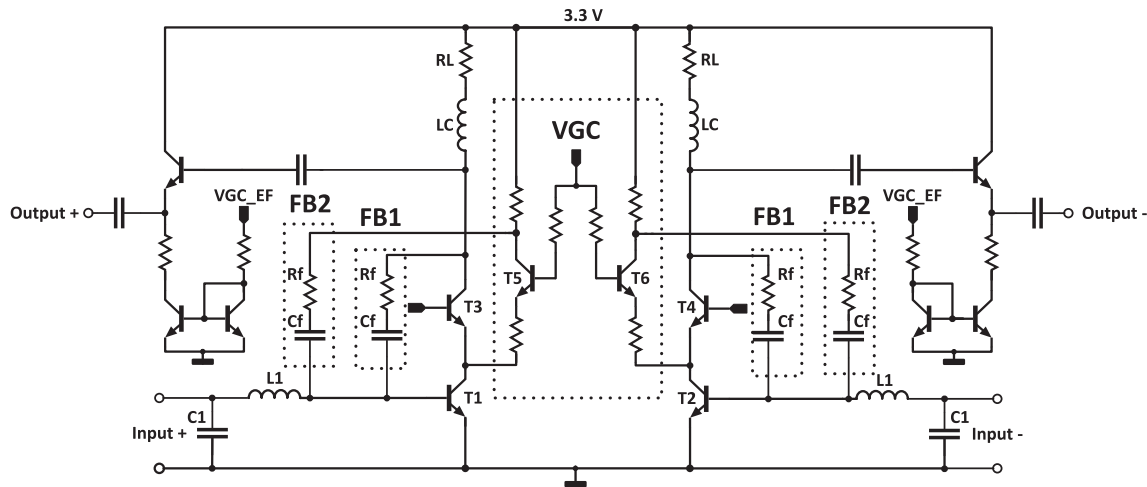


Fig. 3. Schematic of the presented LNA with the variable gain control circuit for input matching and flat gain for all gain control levels. It includes all bandwidth extension methods. Biasing is not shown here.

A combination of several methods enables a gain characteristic of the LNA, which meets the 3 dB-criterion over a very large frequency range. After the description of the basic topology, the used techniques are presented in detail, namely the shunt feedback, the shunt peaking and a special tuned emitter follower stage (EF).

Basic topology

The basic topology of the LNA is the well-known cascode (CC). For broadband amplifiers in general, it is one of the favorite basic topologies, because of its reduced Miller effect. The Miller effect is mainly caused through the parasitic Miller-Capacitance C_m between the collector and the base node of a common emitter stage (CE). The reduction of this capacitance is achieved through the low input impedance of a common base stage (CB), which is stacked onto the collector node of the CE. Furthermore, this reduces the time constant $\tau \approx R_L \cdot C_m$ and enhances, in the same way, the bandwidth of the LNA. A drawback of the topology-based bandwidth enhancement is the slightly higher noise figure. The reason for that is the additional noise contribution of the CB stage. Additionally, the isolation of the LNA benefits also from the stacked CB transistor, which is important for a VNA. The gain of a basic CC can be described (based on [6, 7]) in a good approximation with the following expression:

$$A_V(s) = -g_m \cdot (Z_{out,CC}(s) || Z_L(s)). \tag{1}$$

In equation (1), g_m is the transconductance, $Z_{out,CC}(s)$ describes the output impedance of the CC and $Z_L(s)$ stands for the load impedance, which is seen by the CC. Equation (1) shows that the gain of the basic CC depends directly from the load impedance $Z_L(s)$, and indirectly from the load current, which affects the transconductance g_m .

Techniques for bandwidth extension

As mentioned above, a combination of various techniques is necessary to reach a bandwidth over several octaves. The first technique for bandwidth extension is a shunt feedback (FB1) from the CC output node to the base of the common emitter circuit of the CC, which can be seen in Fig. 3. The shunt feedback consists of a series connection of a TaN resistor R_f and a MIM

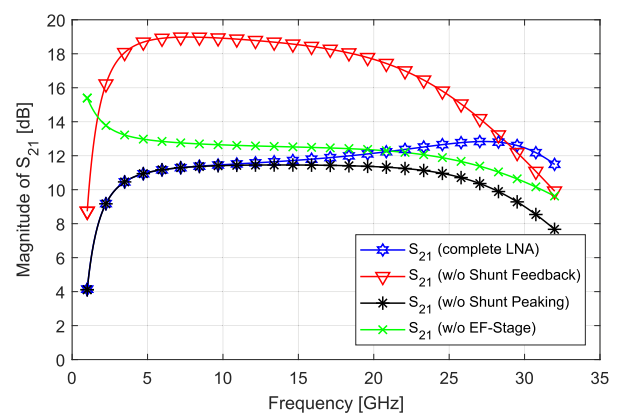


Fig. 4. Simulated influences of the different bandwidth extension methods to the gain function of the LNA. To demonstrate the impact of each method, the respective circuit part was deactivated during the simulation.

capacitor C_f . A CC stage in its basic configuration exhibits a high gain at low frequencies. To flatten the gain at low frequencies, the proposed shunt feedback (FB1) can be used, because it reduces the gain peak of the basic CC at low frequencies and pushes simultaneously the 3 dB cut-off frequency towards a higher range. This behavior can be observed by comparing the simulation results of Fig. 4. Gain and bandwidth are coupled by the gain-bandwidth product (GBW) [7]. Therefore, the gain reduction results in a higher bandwidth.

To improve the frequency bandwidth further, shunt peaking is implemented in the LNA. In case of shunt peaking, an additional inductance L_C is implemented in series with the collector branch of the CC, as can be seen in Fig. 3. This inductance is realized as a spiral inductor on the top metal layer of the used B7HF200 technology. To get an accurate simulation model for the shunt peaking inductance, the spiral inductor was simulated with the 2.5-D simulator from Sonnet Software, Inc. For higher frequencies, the impedance of the inductor L_C increases and compensates the reduction of the output impedance $Z_{out,CC}(s)$, which is caused by the equivalent capacitance C_{eq} on the output of the CC. The equivalent capacitance C_{eq} summarizes all capacitances on the CC's output. This results in an increased gain

over a wider frequency range, compared to the basic CC circuit. With the right choice of the value of the inductor L_C , the impedance of L_C helps to reach a flat gain variation over the extended frequency range. From the time domain point of view, a higher bandwidth can be achieved by reducing the time constant τ of the CC output [8]. In this case, especially the rise time $t_{C_{eq}}$ of the parasitic capacitor C_{eq} is important [8]. Through the delayed current flow caused by the inductor L_C , the current-need of the parasitic capacitance can be better fulfilled [8]. Hereby, the time constant on the output of the CC can be reduced and the overall bandwidth can be extended. For simplification, the following examinations for shunt peaking is done on a single-ended CC. The load impedance Z_L consists of a series connection of the load resistance R_L and the added inductance L_C , which are in parallel to the parasitic capacitances of the CC output. All capacitances are summarized in C_{eq} . The impedance Z_L of the resulting equivalent circuit can be expressed according to [8] as follows:

$$Z_L(s) = (sL_C + R_L) \parallel \frac{1}{sC_{eq}}, \quad (2)$$

which can be rearranged in

$$Z_L(s) = \frac{R_L[1 + s(L_C/R_L)]}{1 + sR_L C_{eq} + s^2 L_C C_{eq}}. \quad (3)$$

If the magnitude of (3) is formed, the effect of the additional inductance L_C can be further investigated:

$$|Z_L(j\omega)| = R_L \sqrt{\frac{(\omega L_C/R_L)^2 + 1}{(1 - \omega^2 L_C C_{eq})^2 + (\omega R_L C_{eq})^2}}. \quad (4)$$

By a closer view on (4), two additional terms are perceptible related to the basic function of a RC-circuit at the output. In detail, these are the term $(\omega L_C/R_L)^2$ in the numerator and the term $(1 - \omega^2 L_C C_{eq})^2$ in the denominator. Both terms yield to a higher bandwidth. The first one increases the impedance $|Z_L(j\omega)|$ for rising frequencies and the second one increases the impedance $|Z_L(j\omega)|$ as well for frequencies below the resonance frequency of the LC-circuit [8]. Additionally, the influence of shunt peaking to the gain function of the LNA is shown by simulation. By comparing the corresponding simulated curves in Fig. 4, the bandwidth extension through shunt peaking can be observed.

With EF, the bandwidth can be further increased, as shown in Fig. 4. For this, the EF has to be loaded capacitively and moreover, specific biasing conditions must be met. The goal is a RLC series resonant behavior of the EF [9]. This leads to a gain peak at high frequencies. In combination with the gain distribution of the above described enhanced CC, the overall gain bandwidth is considerably increased, as can be seen in Fig. 4. Different to [9], the EF is placed at the output rather than at the input. This allows a much better input matching, which is important for a VNA. The EF can be seen in Fig. 3 with a current mirror biasing, which realizes the second VGC functionality (VGC_EF). To understand why the EF exhibits gain under specific conditions, it is necessary to analyze the dominant parts of the input and output impedance and the resulting behavior of the transfer function. The input impedance z_i (see Fig. 5) of a single-ended emitter follower

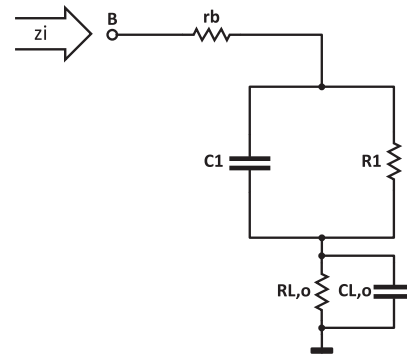


Fig. 5. Equivalent circuit of the input impedance z_i of an EF with capacitively loaded output $C_{L,o}$ [7].

consists in a good approximation of a series connection with the series base resistance r_b , a load resistor $R_{L,o}$ and a parallel connection, which can be represented by an equivalent resistor R_1 and a capacitor C_1 [7]. The equivalent circuit is shown in Fig. 5. According to [7], the resulting expression for the equivalent input impedance z_i is

$$\begin{aligned} z_i &= r_b + \frac{(1 + g_m R_{L,o}) r_\pi}{1 + s \frac{C_\pi}{1 + g_m R_{L,o}} (1 + g_m R_{L,o}) r_\pi} + R_{L,o} \\ &= r_b + \frac{R_1}{1 + s C_1 R_1} + R_{L,o}. \end{aligned} \quad (5)$$

In equation (5), r_π represents the small signal input resistance, whereas C_π is the parasitic capacitance parallel to r_π . The small signal resistor r_b stands for the series resistance of the base node.

For the equivalent elements R_1 and C_1 the following expressions can be determined [7]:

$$R_1 = (1 + g_m R_{L,o}) r_\pi, \quad (6)$$

and

$$C_1 = \frac{C_\pi}{1 + g_m R_{L,o}}. \quad (7)$$

If the output of the EF is capacitively loaded, which is represented in Fig. 5 by the capacitance $C_{L,o}$, the input impedance of the EF exhibits also a capacitive behavior, because the capacitor $C_{L,o}$ on the output is in parallel to the load resistor $R_{L,o}$, which is a series component of the input impedance. If the condition $1/g_m < (R_s + r_b)$ is met through a high biasing current and a large impedance of the source R_s , which is presented here through the output of the CC, the EF acts for high frequencies on its output like an inductor [6, 7, 9]. As a result, the EF exhibits the same behavior as a RLC circuit. For simplification and focusing on the effect itself, a single-ended version of the EF is assumed in the following mathematical expressions. As shown in [9], the function of the gain can be approximated with the following expression for a single-ended EF:

$$A(j\omega) \approx \frac{1}{1 + j\omega \left[r_b C_\mu \left(\frac{1}{g_m} + \frac{r_b}{\beta} \right) C_{L,o} + \frac{r_b C_{L,o}}{\omega_T R_{eq,o}} \right] - \omega^2 \frac{r_b C_{L,o}}{\omega_T}}. \quad (8)$$

In equation (8), $R_{eq,o}$ stands for the parallel connection of the output

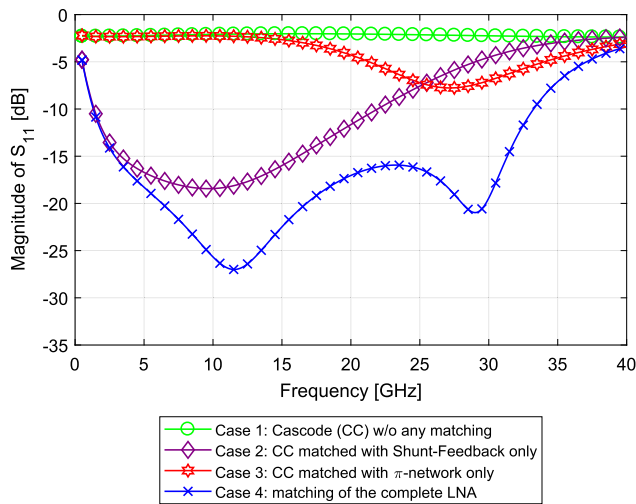


Fig. 6. Simulated influences of the different used matching methods on the magnitude of S_{11} .

resistance r_o of the transistor and the resistive part of the load $R_{L,o}$. C_μ is the parasitic capacitance between base and collector. From equation (8), the resonance frequency ω_r can be determined to

$$\omega_r = \sqrt{\frac{\omega_T}{r_b C_{L,o}}} \tag{9}$$

As a result, equation (9) shows that the frequency with the maximum gain peak is anti-proportional to the load capacitance $C_{L,o}$ and depends on the collector current density j_C , which influences the transit frequency ω_T of the emitter follower. In the shown LNA, the EF shifts the gain peak up to approximately 28 GHz, as can be seen in Fig. 4.

Broadband input matching

Just as with the gain function, for a wideband input matching over several decades, a combination of different matching mechanisms is necessary. For the presented LNA, two different methods are combined as can be seen in Fig. 3. To achieve an input matching for the desired bandwidth from 1 to 32 GHz, a π -network is realized at the input of each branch of the quasi-differential CC and additionally, a second method in form of a shunt feedback (FB1) is implemented, which can be seen in Fig. 3. The second method is also used for bandwidth extension of the gain function, as described before.

The major impact on the input matching function comes from the feedback branch (FB1), which is implemented between the output node and the input node of the CC on each half-circuit of the LNA. In Fig. 6, the effect of the shunt feedback (FB1) can be seen by the comparison of the curve (Case 2) with the matching function of the completed LNA (Case 4) with all matching methods included. By a qualitative comparison of both curves, it becomes obvious that for the frequency range below approximately 23 GHz the matching is mainly determined by the shunt feedback (FB1). The CC itself has an input impedance Z_{in} , which exhibits a strong influence from its base-emitter capacitance C_π . In Fig. 7, this behavior is shown in Case 1 (see also Fig. 6, Case 1), where the CC is simulated without any matching. The shunt feedback leads to a reduction of the imaginary part of the input impedance Z_{in} for low and medium frequencies, as can

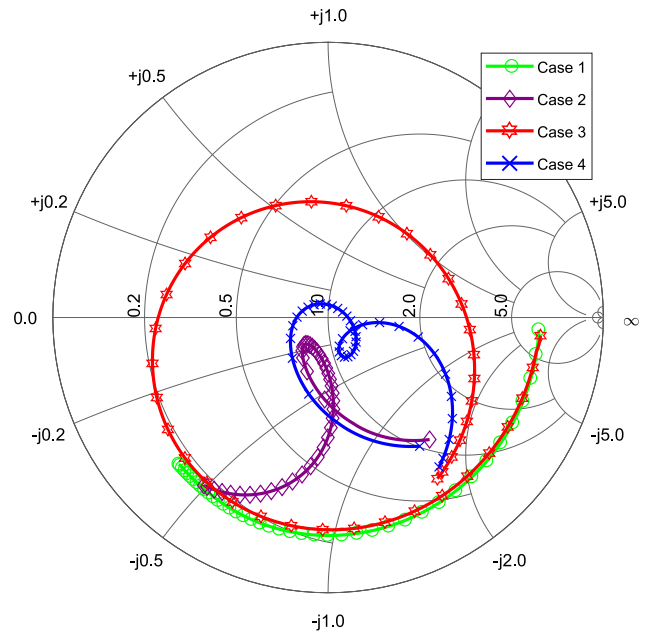


Fig. 7. Simulated influences of the different used matching methods including the phase. The “Cases” are named in the legend of Fig. 6.

be seen by the comparison of Case 1 with Case 2 in Fig. 7. Additionally, the shunt feedback reduces the resistive part of Z_{in} , which is shown in Fig. 7, Case 2. The explanation for this is that for small signal conditions, the feedback branch is in parallel to the base-emitter resistor r_π and to C_π . According to [10], this can be expressed by:

$$Z_{in} \approx R_f \parallel Z_\pi \parallel \frac{R_f + R_L}{g_m R_L} \tag{10}$$

Here, Z_π describes the parallel circuit of the parasitic base-emitter resistance r_π with the base-emitter capacitance C_π on the CC input. As a result, the resistive part of the feedback branch lowers the real part of Z_{in} for low and medium frequencies as shown in Fig. 7, Case 2. By a careful choice of R_f the input impedance can be shifted near to the matching impedance Z_0 for low and medium frequencies. Furthermore, the shunt feedback (FB1) leads to a more broadband characteristic of the input impedance Z_{in} , what will be apparent from the consideration of Case 2 in Fig. 7. The resulting characteristic of the input matching is shown in Fig. 6, Case 2. For frequencies higher than 23 GHz, the matching is not good enough. To achieve a more broadband matching, an additional LC-network is implemented at the input, which forms together with Z_{in} and the impedance of the feedback branch a π -network. The LC-network consists of the inductor L_1 and the MIM capacitor C_1 . The π -network influences the matching only in a limited range, as can be seen in Fig. 6. The red curve (Case 3) shows the simulated influence of the π -network in absence of the feedback branches. It consists in the simulated case only of the MIM capacitor C_1 , the inductor L_1 and the parasitic base-emitter capacitance of the common emitter transistors T1 and T2, respectively. In the realized circuit, the capacitive behavior of the feedback branches has an impact to the overall capacitance of the π -network’s branch at the input node of the

CC. Furthermore, it is obvious from Fig. 6, Case 3 that the π -network is tuned in this way that its influence to the matching function appears in the frequency range from 15 to 40 GHz. The goal of the additional LC-circuit at the LNA's input is to compensate the capacitive characteristics of the CC with a shunt feedback to a certain extent and additionally move the resistive part of Z_{in} more to the optimal matching point. Both effects of the additional LC-network can be seen in Case 3 in Fig. 7, where only the LC-network is implemented at the LNA's input without the feedback branches. For low frequencies, the LC-network does not have an effect in this constellation. The plotted curves in Fig. 6, Case 4 and in Fig. 7, Case 4, show the resulting matching of the LNA, when both methods are implemented. Unlike the traditional implementation of the shunt feedback (FB1), the MIM capacitor C_f in the feedback branch is not only implemented to separate the input- and the output-biasing. In this case, its value would be very high. For the presented LNA, the value of the capacitor C_f is chosen around $C_f = 200 \text{ fF}$. This value was carefully chosen during the design process to place the zeros in the linear matching function in this manner that the matching is best over the desired frequency range.

Extended variable gain control circuit

In the proposed design, the standard CC topology is enhanced with a special circuit (see three dotted boxes named with FB2 and VGC in Fig. 3), which provide an adjustable variable gain and make sure that the input matching is good for all gain levels over a wide frequency range. This behavior is reached due to the additional shunt feedback (FB2) in the gain control branch, which is shown in Fig. 3 in the left and right dotted box. To improve the isolation inside the VNA, a second VGC circuit (VGC_EF) is implemented in the emitter follower output stage of the LNA, as shown in Fig. 3 on the left- and right-side.

The reason for the need of the additional shunt feedback branch (FB2) in the VGC circuit becomes clear by a closer view on the mechanism, which occurs if the transistors T5 & T6 of the VGC circuits become conductive. By becoming a lower load impedance for the common emitter transistors T1 & T2, the gain of the CC decreases. Because of the strong effect of the shunt feedback on the input impedance Z_{in} , the matching would also be hardly degraded, if the feedback branch becomes more and more ineffective, when the current through the upper part of the CC is shifted into the VGC circuit. To compensate the declining effect of the original shunt feedback (FB1), a second feedback branch (FB2) is implemented from VGC circuit to the base node of the common emitter transistor of the CC. The values of the resistor and the capacitance of the second feedback (FB2) are equal to the ones of feedback (FB1). The additional feedback (FB2) is implemented on both half-circuits of the differential CC. To keep the influence of the feedback branch on the input impedance relatively constant over all gain levels, the values of the resistors at the collectors of transistors T5 & T6 are equal to the value of the resistors R_L on top of the cascode. The measured results are shown in the next chapter.

Stability of the LNA circuit

The impedance of a DUT, which is measured with the monolithic integrated VNA, is not in every case 50Ω . Therefore, it can cause instabilities inside the LNA. To ensure that the LNA is stable under all possible load conditions, the K-Factor method, sometimes called the Rollet-Factor, is an often used method. The DUT connected to the LNA's input can cause instability if the

LNA is not unconditionally stable. The output load connected to the LNA can cause instability as well, if the LNA is not stable under all conditions. Especially, the use of an EF as output stage of the LNA, that acts as bandwidth extension in the before described manner, is a potential source of instability. The reason for this is the resulting RLC-resonant behavior, as mentioned above. The used MIM-capacitor at the output of the EF has a major impact to the resonant behavior of the EF. Its value must carefully be chosen. Together with the inductance of the connection lines, it can lead to oscillations and as a result, the whole circuit becomes unstable [9]. To avoid this, the connection between the CC's output and the input of the EF is made as short as possible, to reduce the parasitic inductance to a minimum. This avoids possible oscillations, if the connection is short enough. With K-Factor simulations, the stability is checked. The results can be seen in Fig. 17 in the section "Characterization results". As explained in [11, 12], the circuit is unconditionally stable, if the criteria

$$K > 1, \quad |S_{11}| < 1 \quad \text{and} \quad |S_{22}| < 1, \quad (11)$$

are fulfilled. Because the Rollet-Factor determines only instabilities caused by external loads, a further analysis is necessary to detect instabilities, which are caused through slightly negative impedances inside a stacked topology like the CC. The CC is potentially unstable, because of its CB transistor on its top. So, special care is spent, to ensure a low ohmic AC-coupled connection to ground.

To detect instabilities inside the stacked CC circuit, without affecting it, a special tool is necessary, the so-called *S-Probe* stability simulation [13]. The results of the S-Probe check at the base node of the CB transistors can be seen in Fig. 18 in the section "Characterization results".

Influence of process-tolerances

In the fabrication process, the values of the single components inside the chip vary from their ideal value, which were used in the simulation. Two reasons are responsible for that. The first and most powerful reason is the process variation over the wafer. Therefore, chips from far separated places on the wafer exhibit strongly different deviations from the ideal value. Especially for components like resistors and capacitors, the variation can be far more than $\pm 10\%$. This leads to variations in the performance parameters of the realized circuit. The second source of process tolerances are the deviations between components inside a single chip, the so-called "mismatch". They are less strong than the process variations, but due to the fact that both types of variation occur during the fabrication process, the overall tolerances depend on both. The effect of these two variations on the performance parameters can be determined through a Monte Carlo (MC) simulation.

The MC simulation is done with 1000 sweeps. Both types of variations are done at the same time. In Fig. 8, the result of the MC simulation for the S_{11} -parameter is shown. For the correct interpretation of the simulation results, it is important to note that the density of the different S_{11} -plots is not the same along the y-axis. Therefore, the probability becomes less to the vertical edges of the family of curves. To make this visually clear, the mean-value is calculated and plotted for each simulated frequency point. The red thick solid curve shows the mean values. As a value for the ordinary deviations, the standard deviation was calculated

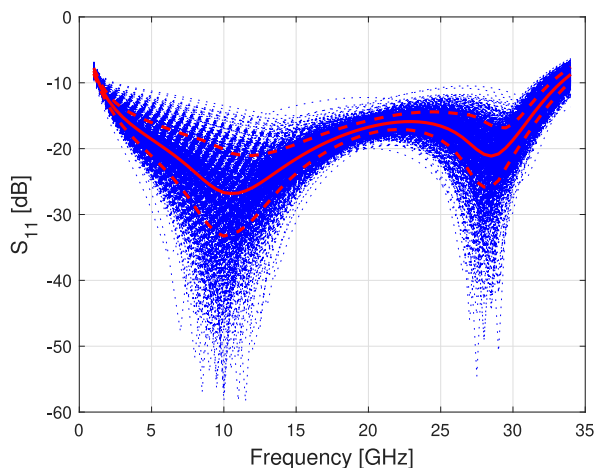


Fig. 8. Monte Carlo simulation of the input matching S_{11} in [dB] over process- and mismatch-variations. The Monte Carlo simulation contains 1000 sweeps.

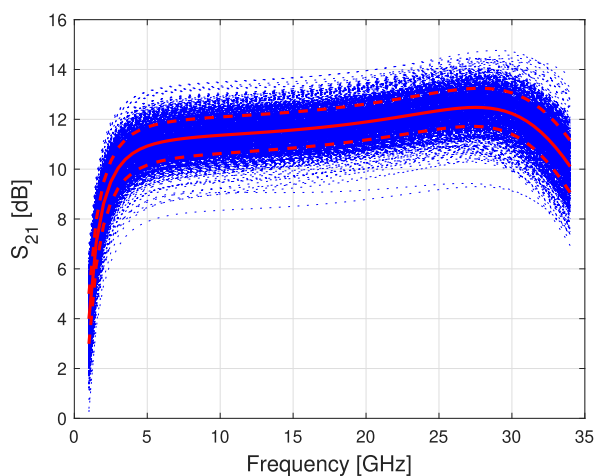


Fig. 9. Monte Carlo simulation of the LNA's gain S_{21} in [dB] over process- and mismatch-variations. The Monte Carlo simulation contains 1000 sweeps.

for each simulated frequency point over the family of curves and is plotted in the diagram as red dotted curve. The key information, which can be extracted from Fig. 8, is that the matching limit of -10 dB over the desired bandwidth can be adhered. As explained before on the input matching, a MC simulation is also done on the parameter S_{21} . The result of the MC simulation of the gain S_{21} of the LNA is shown in Fig. 9. With the help of the standard deviation and the mean-value, the key information can be extracted that the gain of the LNA varies usually ± 1 dB around the mean value.

RF downconverter

The second key component in the RX Chain of a VNA is the RF Downconverter, which has a lot of influence on the measurement performance of the VNA. The RF Downconverter consists of a Gilbert Mixer with an additional output buffer, as can be seen in Fig. 10. Besides the high CG, which can be achieved with this topology of an active mixer, the double balanced architecture

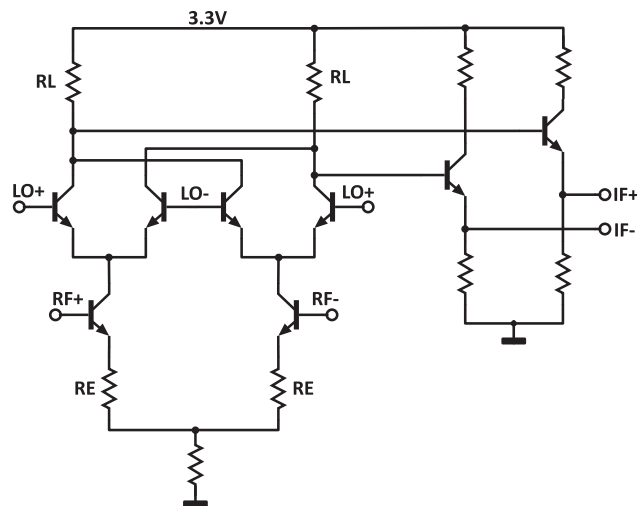


Fig. 10. Simplified schematic of the RF-Downconverter without biasing. On the right side, the IF buffer is shown.

allows a powerful common-mode rejection. In the context of a Multi-Port VNA, it is very important to get a very high isolation between the measurement channels.

Besides the core of the Gilbert Mixer, the output buffer is depicted on the right side of Fig. 10. The buffer improves the gain of the basic mixer core through its high input impedance, because it is in parallel to the load resistors of the Gilbert Mixer. The mixer load itself is realized without the typical parallel MIM capacitors and spiral inductors. These components would result in a strong limitation of the mixer bandwidth. The RF Stage of the Gilbert Mixer has two additional TaN resistors R_E for emitter degeneration. This helps to flatten the CG.

One important property for the performance of the VNA is the gain of the measurement receiver paths, because the gain influences directly the sensitivity of the VNA. The CG itself inside the mixer is mainly determined throughout the mixer's RF-stage, which is in a typical Gilbert Mixer a differential pair. A simplified description of the available CG of the Gilbert Mixer can be given according to [14] by the following equation (12).

$$A_V = -\frac{2}{\pi} \cdot \frac{g_{m_DiffPair}}{1 + g_{m_DiffPair} \cdot R_E} \cdot R_L \tag{12}$$

In equation (12), the resistors R_E for the emitter degeneration are taken into account. This reduces the CG by a factor of $(1/(1 + g_{m_DiffPair} \cdot R_E))$, but improves the linearity of the mixer. In equation (12), a perfect LO square waveform is assumed, which excites the LO switching quad as perfect switches, with an infinitely high slew-rate. For sinusoidal waveforms, as they are typically produced by integrated RF oscillators, the slew rate is lower than for square signals. This leads to a small time frame ΔT per half-wave, where all transistors of the switching-quad are conductive [15]. In this time frame, the small signal current of the RF stage is split into equal portions. Therefore, in the time frame ΔT most of the input signal is converted from differential-mode into common-mode. Thus, for ΔT , no gain is produced on the balanced output node of the differential pair on the RF-Port. To overcome this gain reduction to a large extent, a high amplitude for the LO driving-signal has to be applied, to achieve a high slew-rate. Therefore, the optimal

power level for the LO-signal has to be determined. The optimal power level is measured and is shown in the following chapter “Characterization results” section “Optimal LO power level”.

Characterization results

Setup for single-ended measurements

For characterization, a Keysight PNA-X vectorial network analyzer is used in combination with Z-Probes with 100 μm pitch and GSGSG-pinning. The measurements are done in single-ended configuration, as well as the simulation of the CG, whereas NF and P1dB are simulated in a balanced configuration. The intermediate frequency is 1 GHz. The characterization of the receiver chain is done by the *Scalar Mixer (SMC)* measurement, which is implemented as an option in the PNA-X. The SMC measurement considers in contrast to a normal S-Parameter measurement the frequency translation between the input and the output of the receiver. In the SMC option, standard S-Parameters S_{11} and S_{22} are measured for determining the matching, whereas the CG according to [5] is determined by the ratio of the following wave portions:

$$SC_{21} = \frac{|b_{2_OutputFreq}|}{|a_{1_InputFreq}|} \bigg|_{a_{2_OutputFreq}=0} \quad (13)$$

In equation (13), $b_{2_OutputFreq}$ is the outgoing wave portion of the IF-Port of the receiver on the IF frequency and $a_{1_InputFreq}$ the ingoing wave portion on the RF-Port of the receiver on the RF-Frequency. The calibration of the SMC measurement is done in two steps [5]. In the first step a power calibration of the LO-, RF- and IF-Port is done, to adjust the power level on the respective reference plane, as well as to calibrate the PNA-X’s reference receiver to the respective reference plane’s power level [5]. In the second step, a TOSM calibration of the RF- and IF-Port is carried out. The respective reference plane is set to the tips of the Z-Probes. The chip photo is shown in Fig. 11. The outer dimensions of the fabricated chip are $928 \times 928 \mu\text{m}$.

Conversion gain and input-matching

Figure 12 shows the measured conversion gain SC_{21} and the input matching S_{11} of the receiver chain chip. The CG is greater than 15 dB over a frequency range from 2.1 up to 32 GHz and the 3 dB-criterion is met from 1 GHz on. The input matching is better than -10 dB from 1 to 28 GHz, which is very important for a network analyzer, because calibration and measurement results of the integrated VNA are much more accurate if the input matching is good. The comparison of the measured input matching with the simulated one shows a good agreement in the range between 1 and 25 GHz. Above this frequency range, the geometry of the input transmission lines has an effect, because in simulation the cavity around the input spiral inductors was not considered.

Figure 13 shows the resulting input matching for different gain levels, as well as the resulting CG. Furthermore, Fig. 13 shows an additional isolation through the deactivated EF of the LNA. The measurement results in Fig. 13 shows a matching better than -10 dB up to 18 GHz for all gain levels, which is reached through the additional shunt feedback extension (FB2) in

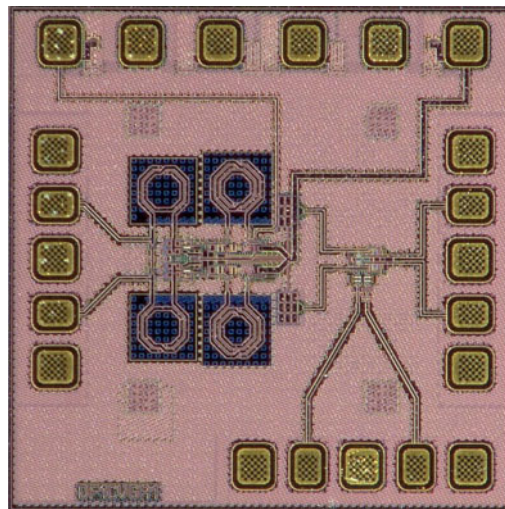


Fig. 11. Chip photo of the designed broadband receiver. The outer dimensions of the fabricated stand-alone chip are $928 \times 928 \mu\text{m}$.

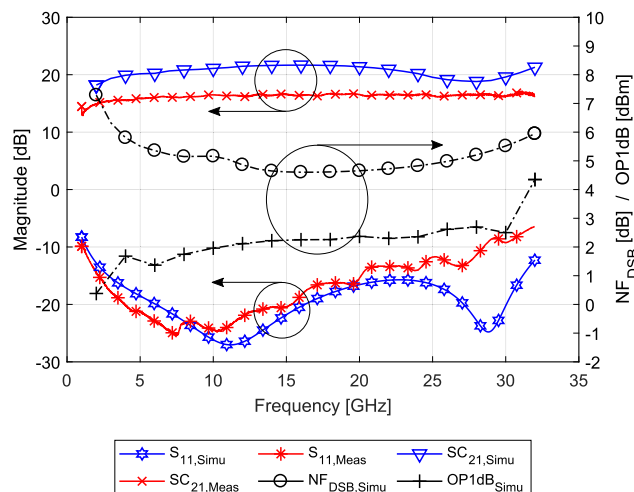


Fig. 12. Characteristics of the whole receiver chain. $S_{11,Meas}$ describes the measured input matching and $SC_{21,Meas}$ the measured conversion gain. Additionally, the simulated input matching $S_{11,Simu}$ and the simulated gain function $S_{21,Simu}$ are shown. Finally, the simulated Double-Side Band (DSB) noise figure $NF_{DSB,Simu}$ and the simulated output referred compression point $OP1dB_{Simu}$ are shown.

the VGC circuit (see Fig. 3). This is very important to avoid reflections back to sensitive materials under test.

Simulation results of noise figure and compression point

In Fig. 12, the simulated noise figure (NF_{DSB}) and the simulated output-referred 1 dB compression point (P1dB) are shown. In case of the NF, the values are between 4.6 and 5.8 dB for 4–32 GHz. The values of P1 dB are between 0.1 and 4.3 dBm in the frequency range from 2 to 32 GHz.

Optimal LO power level

The power level of the LO-Signal has an impact on both, the CG and the noise figure (NF_M) of the downconversion mixer.

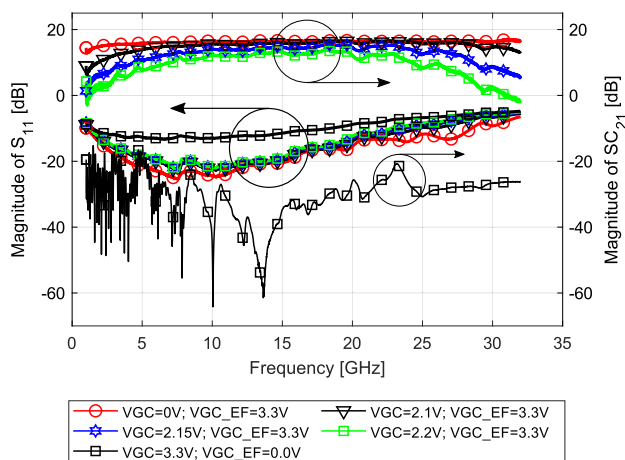


Fig. 13. Measurement results of input matching S_{11} and conversion gain SC_{21} for various gain control levels VGC of the CC circuit of the LNA and VGC_EF of the EF output stage of the LNA.

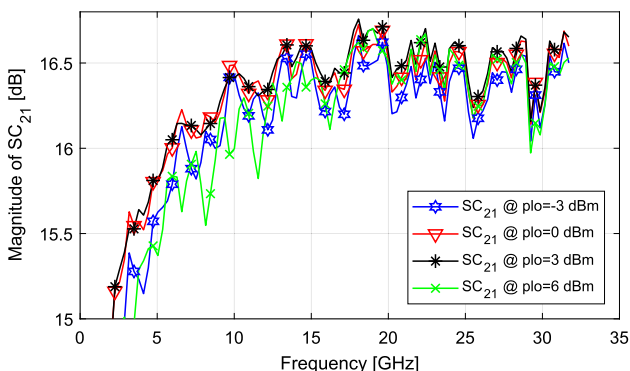


Fig. 14. Measured conversion gain SC_{21} for various power levels on the LO-Port.

Therefore, the optimal LO power has to be determined. In Fig. 14, the conversion gain SC_{21} of the receiver for various power levels is shown. The optimum conversion is reached for power levels between 3 and 6 dBm. For lower power levels, as well as for higher power levels, the conversion degrades.

Isolation

In the following, the results of the isolation measurements are presented. In detail, the LO-to-RF isolation, the RF-to-LO isolation and LO-to-IF isolation. Before the results are presented, the measurement setup, as well as the calibration, is explained.

Measurement setup

The measurement of the receiver’s isolation requires a *true differential* excitation of the receiver’s ports. This means, that a single-ended measurement with a subsequent conversion from nodal into modal S-Parameters is not sufficient in this case. The reason is that the used Gilbert Mixer only works as a double balanced downconverter, if the switching quad is driven with a fully differential signal. The common use of a balun is not preferable in this case, because of the high input bandwidth of the receiver chain. A balun would generate mode conversion, because of its not perfect symmetry over the whole bandwidth. The measurements are done

with a Keysight PNA-X with *iTMSA-Option* (Integrated True Mode Stimulus Application), which is implemented in firmware Option 460. This option allows the interconnection of the two internal sources of the PNA-X to one balanced source. With the help of this interconnection, two balanced ports can be realized. Therefore, the modal S-Parameters can be measured directly and furthermore, the correct excitation of the Gilbert Mixer is possible.

The calibration of an iTMSA-measurement is carried out in three steps. The first step is a power calibration over the whole measurement bandwidth. With a thermal power meter from Rohde & Schwarz & Co. KG (NRP-Z55), the power calibration is done single-ended on source 1 of the PNA-X. In step 2, a 4-Port TOSM-Calibration with a CAL-Substrate is done. By this step, the reference plane is set to the tips of the measuring probes. For the isolation measurement Z-Probes (Z040-K3K) from Cascade Microtech, Inc. are used, which have a pitch of 100 μm and a GSGSG-pinning. According to [5], a third calibration step is necessary, especially for DUTs, which need a perfect differential excitation to have a good differential mode behavior, as well as a good common mode suppression. In general, a symmetrical differential excitation can become unsymmetrical through a not perfect matching, layout inaccuracies or inaccurate contacting [5]. This leads to a phase-skew, which has to be compensated. For determining the phase-skew, on each of the two balanced ports, a sweep of the phase is done in this way that only one of the two single-ended ports of a balanced port is swept in its phase, whereas the other is fixed in its phase. The phase-sweep is done with the highest frequency of the operating band of the receiver chain. By means of the highest isolation, which occurs over the phase-sweep, the deviation of relative phase to the ideal phase-offset of 180° between the two single-ended ports of a balanced port can be determined. The determined phase-skew of the DUT is inserted as an offset in the iTMSA-option of the PNA-X. The proposed receiver did not exhibit any significant phase-skew in the measurement. Therefore, no phase-offset was inserted in the iTMSA-option.

Isolation of LO- to RF-port

The isolation between the LO-Port and the RF-Port is measured by stimulating the LO-Port with a CW-signal with a power level, which has the same value, as it is used in the normal operating mode. Different to the measurement of the CG, the feedthrough power level of the LO-Signal is measured at the RF-Port at the same frequency. In Fig. 15, the lower curve (3) shows the measured LO-to-RF isolation. The measured isolation for the whole input frequency band is equal or better than 60 dB. Such a high isolation is well suited for the application of a monolithic integrated VNA. The suppression of the LO-Signal on the RF-Port is very important to avoid self-mixing of the LO on a poorly matched DUT, which is measured with the integrated VNA. Furthermore, the feedthrough of the RF signal to the LO-Port is measured, because this can lead to superposition in the other integrated VNA channels, since all LO-Ports are connected via a LO distribution network. Especially, a superposition with the reference channel would falsify the measurement results of the monolithic integrated VNA. In Fig. 15, the middle curve (2) shows the measured isolation from RF-Port to LO-Port, for the case that the gain of the LNA is set to its minimum. This means that the gain control voltage VGC (see Fig. 3) is set to 3.3 V and the Emitter Follower is fully disabled ($VGC_EF = 0\text{ V}$). The RF-to-LO isolation is better than 30 dB over the whole input bandwidth. For the low and middle frequency range up to 26 GHz, the isolation is better than 40 dB. As a result,

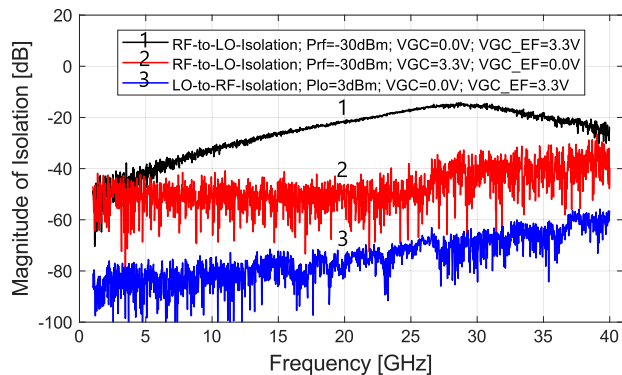


Fig. 15. Measurement results of isolation between LO- and RF-Port and vice versa.

the enhanced gain control function improves the isolation for a disabled measurement channel in the integrated VNA. For the case that the gain of the LNA is set to its maximum, the EF of the LNA is enabled (VGC_EF = 3.3 V), as well as the gain control voltage of the CC has to be set to VGC = 0 V. The resulting RF-to-LO isolation seems to be worse, as can be observed in Fig. 15 at the upper curve (1). But here, the gain of the LNA must be taken into account, which leads to a stronger RF signal on the downconverter's RF-Port. With an input power of -30 dBm on the LNA and the maximum gain level of the LNA, the isolation is better than 20 dB for frequencies below 22 GHz and reaches its minimum of 15 dB at around 28 GHz.

Isolation of LO- to IF-port

A further important feedthrough path is from LO- to IF-Port. Especially, for low measurement frequencies of the monolithic integrated VNA, where the LO frequency has only a small distance to the IF frequency in the spectrum, it is difficult to filter out the harmonics of the LO-Signal. This results in an impure output spectrum, which degrades the measurement performance of the integrated VNA significantly. Therefore, the LO-to-IF isolation has to be as high as possible. In Fig. 16, the measured isolation between the LO- and the IF-Port is shown. Over the whole LO frequency band the isolation is better than 35 dB. The LO power, which was used for the measurement, is 3 dBm on the balanced port.

Stability analysis

K-factor analysis

According to [11, 12] the K-factor can be determined out of the measured or simulated S-Parameters. The K-factor can be expressed according to [11, 12] by

$$K = \frac{1 - |S_{11}|^2 - |S_{22}|^2 + |\det \underline{S}|^2}{2|S_{12}S_{21}|}, \quad (14)$$

with

$$\det \underline{S} = S_{11}S_{22} - S_{12}S_{21}. \quad (15)$$

The simulation results in Fig. 17 show that the LNA is unconditionally stable over the used frequency range, because the conditions in equation (11) are met for all frequencies.

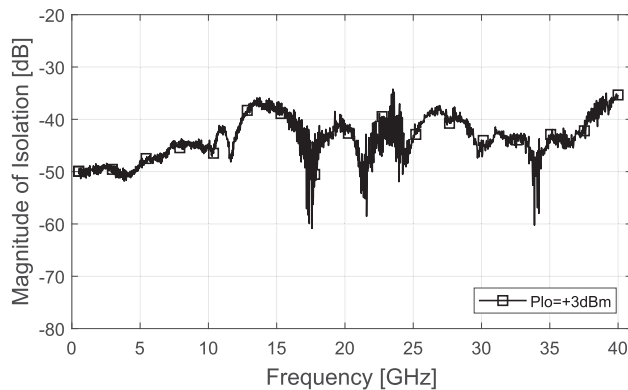


Fig. 16. Measurement results of isolation between LO- and IF-Port.

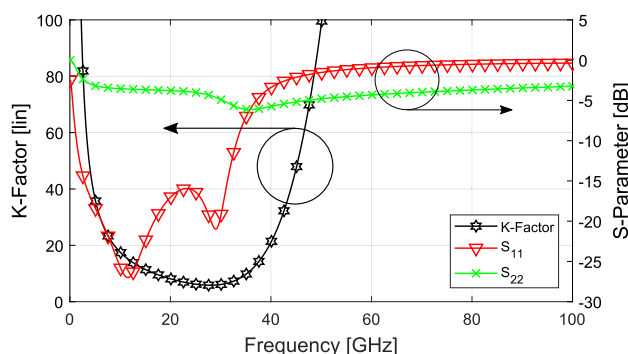


Fig. 17. Results of the simulative stability test with K-factor method of the LNA.

The test is done for a frequency range of 100 MHz up to 100 GHz to ensure, that neither the relevant higher harmonics nor subharmonics can cause an instability. Note, that in Fig. 17 the K-Factor for high frequencies is too high for plotting, but it is simulated until 100 GHz.

S-probe analysis

With the help of the S-Probe, the input reflection coefficient $\Gamma_{IN}(\omega)$ and the output reflection coefficient $\Gamma_{OUT}(\omega)$ can be determined for every node inside a circuit without split up the single parts. Finally, by using the simulated reflection coefficients $\Gamma_{IN}(\omega)$ and $\Gamma_{OUT}(\omega)$, the Nyquist stability criterion can be determined over frequency. For this purpose, the product of $\Gamma_{IN}(\omega) \cdot \Gamma_{OUT}(\omega)$ has to be plotted. If the resulting curve encircles the point (1,0) clockwise, this indicates an instability. This is equivalent to poles in the right-half plane in the Pole-Zero-Plots, as it is typical for oscillators. In Fig. 18, the results of the stability test with the differential S-Probe is shown. Because the plotted product of $\Gamma_{IN}(\omega) \cdot \Gamma_{OUT}(\omega)$ does not nearly encircle clockwise the point (1,0) for any frequency, the tested node is stable.

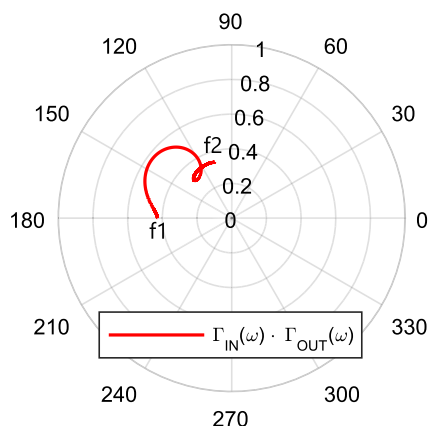
State-of-the-art comparison

The results are compared in Table 1 with some previous designs of other authors.

The bandwidth of over five octaves is outstanding compared with [16–19]. Furthermore, the max. gain deviation is comparable to the other designs, but over a much wider frequency range. The measured current consumption at a supply voltage of 3.3 V has a

Table 1. Comparison of the receiver chain with previous works

Reference	[16]	[17]	[18]	[19]	This work
Technology	CMOS	CMOS	BiCMOS	CMOS	SiGe
BW [GHz]	3.1–10.6	21–29	1–7	3.1–10.6	1–32
max. CG [dB]	29.7	23.7	26	73.5	16.6
Δ CG [dB]	2.1	± 1.4	NA	NA	± 1.5
NF [dB]	5.1 (DSB)	4.6	7 (SSB)	8.4	4.6–7.3 (DSB)
Power [mW]	31.5	39.2	57	88.74	217.8

**Fig. 18.** Results of the simulative stability test with a differential S-Probe, at the base node of the CB transistors of the CC inside the LNA. The stability test was done from $f_1 = 100$ MHz to $f_2 = 100$ GHz.

value of 66 mA, which is higher compared with the power consumption of the designs of the other authors. A reason is that in [16, 17] the LNA is in both cases single-ended, whereas the LNA in this work is fully differential. The noise figure (NF) is between approximately 12 and 26 GHz better, compared with [16], but outside this frequency range a little bit higher. In contrast to [19], the NF is better over the comparable frequency range. The designs in [16, 18] show better noise performance for the frequency range up to 7 and 11 GHz, respectively, which can be explained in both cases by the higher gain. The CG itself is less than in the other designs [16–19]. The reason is the enormously expanded bandwidth, which reduces the gain of the LNA through the gain-bandwidth product.

Conclusion

A multi-octave receiver chain has been presented, which is well suited for a front-end of a monolithic integrated vector analyzer. For this application, the key performance parameters of the receiver chain have been highlighted and the necessary design methodology and topology enhancements have been shown in detail, which are necessary to achieve such an enormous bandwidth of five octaves. The result is a CG of max. 16.6 dB, with a very flat deviation and an enormous 3 dB-bandwidth from 1 to 32 GHz. The input matching is better than -10 dB up to 28 GHz. The NF is between 4.6 and 5.8 dB for 4 to 32 GHz and the output referred 1-dB-compression-point is from 0.1 to 4.3 dBm between 2 to 32 GHz. Especially, an enhanced VGC circuit has been proposed, which enables the handling of

measurement signals with strongly different power levels and provides at the same time a good matching that avoids reflections back to sensitive materials under test. This prevents a falsification of the determined S-Parameters of the material under test. Furthermore, a second gain control functionality has been implemented to improve the isolation of the deactivated chains in the VNA. The measured RF-to-LO isolation is 40 dB up to 26 GHz and 30 dB for higher input frequencies. Additionally, the LO-to-RF isolation is higher than 60 dB for the complete frequency range, which is a very good value. The measured LO-to-IF isolation is better than 35 dB over the complete bandwidth. A special focus has been laid on the measurement setup for the determination of the isolation of the fully differential receiver chain. Finally, the influence of the fabrication tolerances onto the performance parameters has been investigated, as well as the optimal LO power level. The proposed fully differential integrated receiver chain allows very broadband integrated VNAs.

References

- Guarin G, Hofmann M, Nehring J, Weigel R, Fischer G and Kissinger D (2015) Miniature microwave biosensors. *IEEE Microwave Magazine*, pp. 71–86.
- Nasr I, Nehring J, Aufinger K, Fischer G, Weigel R and Kissinger D (2014) Single- and dual-port 50–100-GHz integrated vector network analyzers with on-chip dielectric sensors. *IEEE Transactions on Microwave Theory and Techniques* 62(9), 2168–2179.
- Böck J, Schäfer H, Aufinger K, Stengl R, Boguth S, Schreiter R, Rest M, Knapp H, Wurzer M, Perndl W, Böttner T and Meister TF (2004) SiGe bipolar technology for automotive radar applications. *IEEE Bipolar/BiCMOS Circuits and Technology Meeting (BCTM)*, Montreal, Canada, pp. 84–87.
- Vytla RK, Meister TF, Aufinger K, Lukashevich D, Boguth S, Knapp H, Böck J, Schäfer H and Lachner R (2006) Simultaneous integration of SiGe high speed transistors and high voltage transistors. *IEEE Bipolar/BiCMOS Circuits and Technology Meeting, Maastricht, The Netherlands*, pp. 1–4.
- Dunsmore JP (2012) *Handbook of Microwave Component Measurements: with Advanced VNA Techniques*. Chichester, UK: John Wiley & Sons, Ltd.
- Razavi B (2008) *Fundamentals of Microelectronics*. Hoboken, NJ, USA: Wiley.
- Gray PR, Hurst PJ, Lewis SH and Meyer RG (2010) *Analysis and Design of Analog Integrated Circuits*, 5th Edn, international student version. Hoboken and NJ: Wiley.
- Lee T (2004) *The Design of CMOS Radio-frequency Integrated Circuits*, 2nd Edn. Cambridge, New York, Melbourne, Madrid, Cape Town, Singapore, Sao Paulo, Delhi, Mexico City: Cambridge University Press.
- Trotta S, Knapp H, Aufinger K, Meister TF, Böck J, Dehlink B, Simbürger W and Scholtz AL (2007) An 80 GHz bandwidth and 20 dB gain broadband amplifier in SiGe bipolar technology. *IEEE Journal of Solid-State Circuits* 42(10), 2099–2106.
- Rogers J and Plett C (2003) *Radio Frequency Integrated Circuit Design*. Boston & London, US: Artech House, Inc.

- 11 **Ellinger F** (2007) *Radio Frequency Integrated Circuits and Technologies*. Berlin, Heidelberg, Germany: Springer-Verlag.
- 12 **Rollet JM** (1962) Stability and power-gain invariants of linear twoports. *IRE Transactions on Circuit Theory, CT-9*, pp. 29–32.
- 13 **Schmid RL, Coen CT, Shankar S and Cressler JD** (2012) Best practices to ensure the stability of SiGe HBT cascode low noise amplifiers. *IEEE Bipolar/BiCMOS Circuits and Technology Meeting (BCTM), Portland, Oregon*, pp. 1–4.
- 14 **Voinigescu S** (2013) *High-Frequency Integrated Circuits*. Cambridge, New York, Melbourne, Madrid, Cape Town, Singapore, Sao Paulo, Delhi, Mexico City: Cambridge University Press.
- 15 **Razavi B** (2012) *RF Microelectronics*, 2nd Edn. New Jersey, US: Pearson Education.
- 16 **Shi B and Chia MYW** (2010) Design of a CMOS UWB receiver front-end with noise-cancellation and current-reuse. *Proceedings of 2010 IEEE International Conference on Ultra-Wideband (ICUWB 2010)*, pp. 1–4.
- 17 **Lin Y-S, Lee J-H, Huang S-L, Wang C-H, Wang C-C and Lu S-S** (2012) Design and analysis of a 21–29 GHz ultra-wideband receiver front-end in 0.18- μm CMOS technology. *IEEE Transactions on Microwave Theory and Techniques* **60**(8), 2590–2604.
- 18 **Joram N, Wagner J, Sobotta E and Ellinger F** (2015) Fully integrated wideband sub-10 GHz radio frequency front end with active matching. *11th Conference on Ph.D. Research in Microelectronics and Electronics (PRIME)*, pp. 1–4.
- 19 **Park B, Lee K, Choi S and Hong S** (2010) A 3.1–10.6 GHz RF receiver front-end in 0.18 μm CMOS for ultra-wideband applications. *2010 IEEE MTT-S International Microwave Symposium (IMS)*, pp. 1616–1619.



Marco Dietz received the B.E. degree in communications engineering from the Ulm University of Applied Sciences, Ulm, Germany, in 2011, and the M.Sc. degree in electrical engineering (with a focus on high-frequency engineering and microelectronics) from Friedrich-Alexander-University Erlangen-Nuremberg, Erlangen, Germany, in 2013. In 2014, he joined the Institute for Electronics Engineering,

Friedrich-Alexander-University Erlangen-Nuremberg, as a Research Assistant, where he is currently a member of the Team RF Integrated Systems. Since 2015, he has been the Head of the Team. His current research interests include high integrated, silicon-based microwave circuits and systems with multi-octave bandwidth for material characterization and wireless sensor and communication systems for ultra-low power, industrial and biomedical applications. Mr. Dietz received in 2014 one of the IHP-Young-Talent-Awards, sponsored by Freunde des IHP e.V., for his master thesis.



Andreas Bauch studied electronics engineering at the University of Erlangen-Nuremberg, Germany from 2008 to 2013. He received his M.Sc. degree in electrical, electronic and communications engineering from the University of Erlangen-Nuremberg, Germany, in 2013. In 2013, he joined the Institute for Electronics Engineering, Erlangen, Germany, as a Research Assistant and is currently pursuing his Ph.D.

His working fields cover millimeter wave, RF and integrated circuits.



Klaus Aufinger received the Diploma and Ph.D. degrees in physics from the University of Innsbruck, Innsbruck, Austria, in 1990 and 2001, respectively. From 1990 to 1991, he was a Teaching Assistant with the Institute of Theoretical Physics, University of Innsbruck. In 1991, he joined the Corporate Research and Development of Siemens AG, Munich, Germany, where he investigated noise in sub-micrometer bipolar transistors. He is currently with Infineon Technologies AG, Neubiberg, Germany, where he is involved with device physics, technology development, and the modeling of advanced SiGe technologies for high-speed digital and analog circuits.



Robert Weigel received the Dr.-Ing. and the Dr.-Ing. habil. degrees, both in electrical engineering and computer science, from the Munich University of Technology in Germany where he respectively was a Research Engineer, a Senior Research Engineer, and a Professor for RF Circuits and Systems until 1996. From 1996 to 2002, he has been Director of the Institute for Communications and Information

Engineering at the University of Linz, Austria where, in August 1999, he co-founded the company DICE, devoted to the design of RFICs for mobile radio and MMICs for vehicular radar applications. Since 2002 he is Head of the Institute for Electronics Engineering at the University of Erlangen-Nuremberg, Germany. Prof. Weigel has been engaged in research and development of microwave theory and techniques, electronic circuits and systems, and communication and sensing systems. In these fields, he has published more than 900 papers.



Amelie Hagelauer received the Dipl.-Ing. degree in mechatronics and the Dr.-Ing. degree in electrical engineering from the Friedrich-Alexander-University Erlangen-Nuremberg, Erlangen, Germany, in 2007 and 2013, respectively. She joined the Institute for Electronics Engineering of the Friedrich-Alexander-University Erlangen-Nuremberg as a Research Engineer in 2007, where she is involved in

SAW/BAW components, RF-MEMS, packaging technologies and integrated circuits up to 180 GHz. Dr. Hagelauer has been the Chair of MTT-2 Microwave Acoustics since 2015. Since 2016 she is leading a research group on Electronic Circuits.